PNAS RESEARCH ARTICLE | PHARMACOLOGY
BIOPHYSICS AND COMPUTATIONAL BIOLOGY

Molecular basis for chemokine recognition and activation of XCR1

Xuan Zhang[a,1], Roman R. Schlimgen[b,1], Stephanie Singh[a], Michael P. Tomani[a,2], Brian F. Volkman[b,c,3], and Cheng Zhang[a,3]

Affiliations are included on p. 9.

Edited by Ian Wilson, The Scripps Research Institute, La Jolla, CA; received March 20, 2024; accepted October 15, 2024

The X-C motif chemokine receptor XCR1, which selectively binds to the chemokine XCL1, is highly expressed in conventional dendritic cells subtype 1 (cDC1s) and crucial for their activation. Modulating XCR1 signaling in cDC1s could offer novel opportunities in cancer immunotherapy and vaccine development by enhancing the antigen presentation function of cDC1s. To investigate the molecular mechanism of XCL-induced XCR1 signaling, we determined a high-resolution structure of the human XCR1 and G_i complex with an engineered form of XCL1, XCL1 CC3, by cryoelectron microscopy. Through mutagenesis and structural analysis, we elucidated the molecular details for the binding of the N-terminal segment of XCL1 CC3, which is vital for activating XCR1. The unique arrangement within the XCL1 CC3 binding site confers specificity for XCL1 in XCR1. We propose an activation mechanism for XCR1 involving structural alterations of key residues at the bottom of the XCL1 binding pocket. These detailed insights into XCL1 CC3–XCR1 interaction and XCR1 activation pave the way for developing novel XCR1-targeted therapeutics.

XCR1 | XCL1 | cryo-electron microscopy (cryo-EM) | conventional dendritic cells subtype 1 | chemokine receptors

Significance

We report the cryoelectron microscopy structure of the chemokine receptor XCR1 with Gi protein and XCL1. As the only known G protein-coupled receptor for XCL1, XCR1 is a marker for conventional type 1 dendritic cells (cDC1). XCL1 and its closely related paralog XCL2 are the only chemokines with a single disulfide bond, distinguishing them from other chemokines. The XCL1–XCR1 axis is crucial for cDC1 cross-presentation to activate cytotoxic T cells and natural killer cells (NK cells) against viral infection and tumors. Our structure elucidates the molecular mechanisms of how XCL1 specifically binds to and activates XCR1, providing a foundation for designing optimized XCR1 modulators, which may potentiate XCR1 signaling in the tumor microenvironment to promote anti-tumor immunity.

Dendritic cells (DCs) are professional antigen-presenting cells, orchestrating both innate and adaptive immunity. Studies over the past two decades have revealed various subsets of DCs, each with distinct functions (1, 2). Notably, among these subsets, conventional dendritic cells subtype 1 (cDC1s) are the most potent DCs specialized in cross-presentation of exogenous antigens or neoantigens on major histocompatibility complex class I molecules to $CD8^+$ cytotoxic T lymphocytes (CTLs) (3–7). This ability of cDC1s for cross-presentation serves as a pivotal mechanism for initiating CTL responses against viral infections and tumors. The consistent findings from previous studies have underscored an important role of cDC1s in the context of immune checkpoint blockage therapy (1, 2, 8–10). In addition to priming $CD8^+$ T cells, cDC1s can also prime $CD4^+$ T cells, thereby promoting T helper type 1 (T_H1) immune responses, to regulate self-tolerance and anti-tumor immunity (1, 2, 11, 12).

As distinct features characterizing both mouse and human cDC1s, several unique cell surface markers have been identified (1, 2). One of them is the X-C motif chemokine receptor 1 (XCR1, also named GPR5), which is the only G-protein coupled receptor (GPCR) for the X-C motif chemokine ligand XCL1 or lymphotactin (4, 13, 14). XCL1, secreted by activated $CD8^+$ T cells (3) and natural killer (NK) cells (15), among other lymphocytes, functions as a potent chemoattractant specifically for cDC1s expressing XCR1 (16). The XCL1–XCR1 signaling axis regulates the function of cDC1s, effectively shaping the landscape of appropriate and sufficient cytotoxic immune responses that are mediated by CTLs and NK cells (6, 7, 12, 15–17). XCL1 and engineered variants have undergone investigation to augment the efficacy of various anti-tumor therapeutics and vaccines by activating XCR1 (18–23).

Among the four subfamilies of chemokines, CXC, CC, C, and CX_3C, which target over 20 different chemokine receptors, XCL1 is the primary member of the C motif chemokine subfamily and XCR1 is the only receptor identified for XCL1 (24, 25). For CX3C chemokines, CX3CR1 is also the only receptor identified. In contrast, CXC and CC chemokines act on multiple chemokine receptors (CXCRs and CCRs). As an unusual metamorphic protein, XCL1 has the ability of sampling two different native conformations with distinct structural elements under physiological conditions (26–29). Only the monomeric form of XCL1 with a canonical chemokine structure can bind to and activate XCR1. In addition, a unique feature of the canonical chemokine structure of XCL1 and its closely related paralog XCL2 among chemokines is that the unstructured N terminus connects to the globular core region through a single disulfide bond, while all other CXC, CC, and CX_3C chemokines have two disulfide bonds between their N terminus and the

Author contributions: X.Z., R.R.S., B.F.V., and C.Z. designed research; X.Z., R.R.S., S.S., M.P.T., and C.Z. performed research; X.Z., R.R.S., and C.Z. analyzed data; and X.Z., R.R.S., B.F.V., and C.Z. wrote the paper.

Competing interest statement: B.F.V. has ownership interests in Protein Foundry, LLC and XLock Biosciences, Inc. The other authors declare no competing financial interests related to the studies in this paper.

This article is a PNAS Direct Submission.

[1]X.Z. and R.R.S. contributed equally to this work.

[2]Present address: Department of Pediatric Rheumatology, University of Rochester Medical Center, Rochester, NY 14642.

[3]To whom correspondence may be addressed. Email: bvolkman@mcw.edu or chengzh@pitt.edu.

This article contains supporting information online at https://www.pnas.org/lookup/suppl/doi:10.1073/pnas.2405732121/-/DCSupplemental.

Published November 20, 2024.

core region (Fig. 1*A*) (26). Upon binding to XCR1, XCL1 activates downstream signaling pathways mainly through the heterotrimeric G_i protein (14). For many chemokine receptors, in addition to G_i, β-arrestins have been shown to play critical roles in their signaling, leading to receptor internalization (30) and the chemotaxis of leukocytes (31). However, the internalization of XCR1 does not require β-arrestins (32). Therefore, the role of β-arrestins in regulating XCR1 signaling is still not clear.

To date, only a limited number of engineered XCL1 variants have been identified as synthetic XCR1 ligands. How XCL1 interacts with and activates XCR1 on a molecular level is still largely unknown. Previous studies from Kroczek lab (33) and Volkman lab (34) have examined the functional impacts of various mutations of XCL1 and XCR1 in the XCL1–XCR1 signaling axis, providing molecular insights into the key interactions between XCL1 and XCR1. In this study, as an initial step for our effort of developing XCR1 ligands with desired pharmacological properties to investigate XCR1 signaling in various disease settings, we report the cryo-EM structure of a human XCR1–G_i signaling complex with an engineered XCL1, named XCL1 CC3 (35), at an overall resolution of 3.1–Å. Together with mutagenesis studies, the structure reveals the molecular details of the binding pocket in XCR1 for the N-terminal segment of XCL1 CC3, which is the primary region of XCL1 responsible for receptor activation (35). The distinctive configuration of the binding pocket determines the selective XCL1 recognition by XCR1. Structural comparison analysis suggested a receptor activation mechanism involving conformational changes of XCR1 residues at the bottom of the XCL1 CC3 binding pocket. We anticipate that a comprehensive understanding of the molecular interactions governing XCL1 binding and XCR1 activation can facilitate the development of new XCR1-targeted therapeutics, not only for cancer but also for various inflammatory conditions.

Results

Overall Structure of the XCL1–XCR1–G_i Complex. Our previous studies have suggested that XCL1 is an unusual metamorphic protein that can automatically interconvert between the canonical chemokine structure and an all-β-sheet dimer structure (26–29). To stabilize the monomeric canonical chemokine structure of XCL1 for XCR1 binding, we used a XCL1 variant, XCL1 CC3, by introducing two mutations, V21C and V59C, to human XCL1 following our previous study (35) (Fig. 1*B*). In that study, we have demonstrated that the two cysteine residues C21 and C59 within the globular core region of XCL1 CC3 formed a disulfide bond to stabilize the canonical chemokine structure of XCL1, allowing it to function as a canonical chemokine agonist of XCR1 (35) (*SI Appendix*, Fig. S1*A*). Notably, XCL1 CC3 retains a single disulfide bond between the flexible N-terminal region and the core region, distinguishing it from other CXC, CC, and CX_3C chemokines that have two such bonds (Fig. 1*A* and *SI Appendix*, Fig. S1*A*). In the current study, we tested the agonistic action of XCL1 CC3 by measuring the recruitment of β-arrestin2 or an engineered version of Gi, miniG_i(36), to XCR1 as a result of receptor activation. The results confirmed that the potency of XCL1 CC3 is comparable to that of the WT XCL1 in both assays (Fig. 1*C*).

To enhance the stability of the XCL CC3–XCR1 complex for high-resolution cryo-EM data collection, we linked the C-terminal

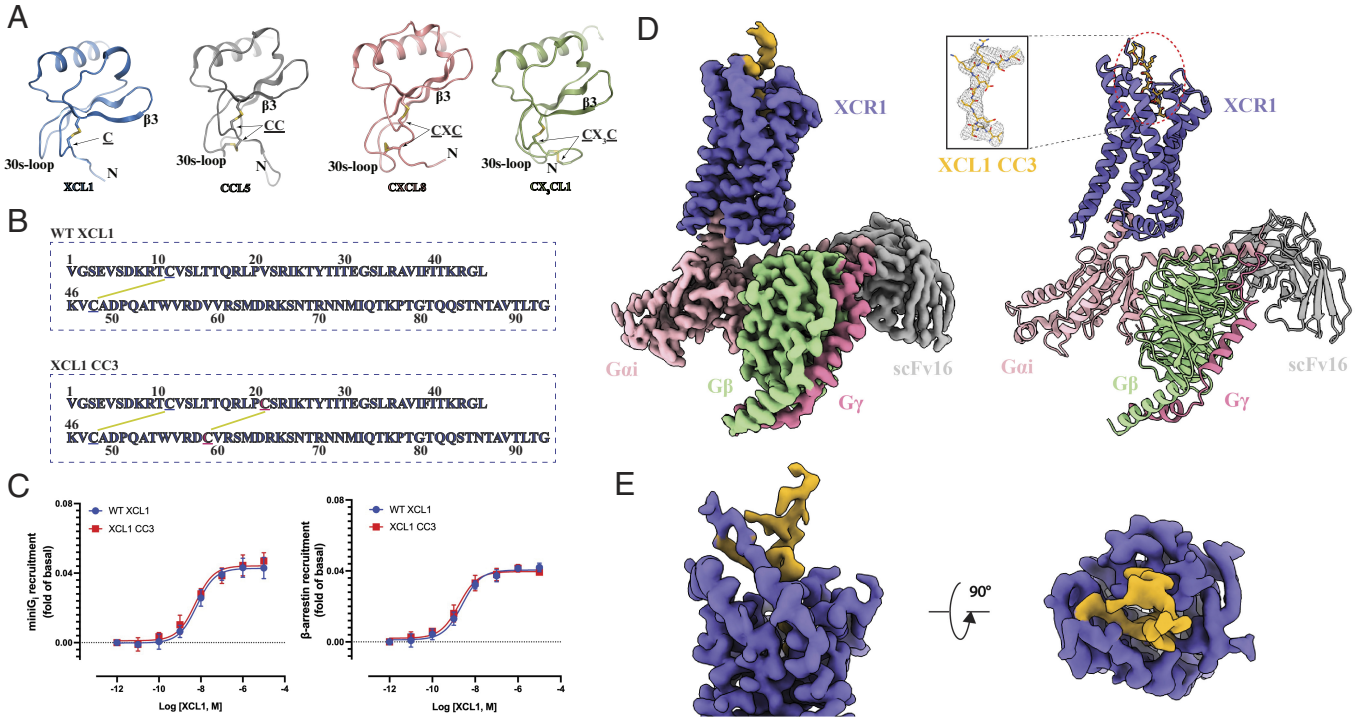

Fig. 1. XCL1 CC3 and overall structure of the XCL1 CC3–XCR1–G_i complex. (*A*) Structural comparison of chemokines from four difference chemokine subfamilies. The structures of XCL1 (PDB ID 2NYZ), CCL5 (PDB ID 5COY), CXCL8 (PDB ID 5D14), and CX_3CL1 (PDB ID 3ONA), which belong to the C, CC, CXC, and CX_3C subfamilies of chemokines, respectively, are shown in blue, dark gray, pink, and green, respectively. In all chemokines except for XCL1, there are two cysteine residues at the N-terminal region, forming two disulfide bonds with cysteine residues in the 30 s-loop and β3 regions, respectively. In XCL1, the disulfide bond with the 30 s-loop is absent. (*B*) Sequences of wild type XCL1 (WT XCL1) and XCL1 CC3. The two cysteine mutations V21C and V59C in CC3 XCL1 are highlighted in red. The yellow lines indicate disulfide bonds. (*C*) Functional characterization of WT XCL1 and XCL1 CC3 by Bioluminescence Resonance Energy Transfer (BRET) assays. Both ligands show similar potencies in miniG_i and β-arrestin recruitment measured by BRET assays. Data are means ± SEM. for n = 3 or more. (*D*) cryoelectron microscopy (Cryo-EM) density and overall structure of the XCL1 CC3–XCR1–G_i complex. XCL1 CC3 and XCR1 are colored in yellow and slate, respectively. $G_{\alpha i}$, G_β, and G_γ subunits are colored in salmon, green, and pink, respectively. ScFv16 is colored gray. (*E*) Cryo-EM density of XCL1 CC3 and the extracellular region of XCR1 after local refinement. The cryo-EM density maps in *D* and *E* are contoured at the level of 1.4-2.0.

end of XCL1 CC3 to the N-terminal end of XCR1 with a highly flexible 40-amino acid linker. This was designed to increase the local concentration of the ligand while still allowing XCL1 CC3 and XCR1 the freedom to move relative to each other. A similar strategy has been used to obtain cryo-EM structures of the signaling complexes of CX_3CR1 (37) and CCR5 (38). Our functional assays demonstrated that the fusion protein induced β-arrestin recruitment at levels comparable to those observed with the WT XCR1 (wtXCR1) when stimulated with free XCL1 CC3 (*SI Appendix*, Fig. S1*B*). Both the fusion protein and wtXCR1-mediated recruitment were effectively inhibited by the chemokine antagonist vMIP-II (*SI Appendix*, Fig. S1*B*). These findings suggest that the fused XCL1 CC3 retains its agonistic activity, capable of activating its associated XCR1. This fusion protein was coexpressed together with a dominant negative version of human G_i (39) using a NanoBit tethering strategy in insect Sf9 cells (40). We also used an antibody fragment, scFv16, which has been developed previously to stabilize the G_i heterotrimer (41). The structure of the XCL1 CC3–XCR1–G_i–scFv16 complex was determined by cryo-EM to an overall resolution of 3.1–Å (Fig. 1*D* and *SI Appendix*, Fig. S2) and Table. S1.

The clear cryo-EM density allowed the modeling of XCR1 from P21 to Q304, encompassing the 7 transmembrane helices (7-TMs) and all the extracellular and intracellular loops (ECLs and ICLs) in the structure. The overall structure of XCR1 resembles those of other chemokine receptors. For XCL1 CC3, the density is less clear. To improve the density, we further performed local refinement on the XCLl CC3 and XCR1 complex. However, despite observing clear density for the N-terminal region of XCL1 CC3, the density for its globular core region was still weak and fragmented after local refinement, making it challenging to model even the main chain of the globular core of XCL1 CC3 (Fig. 1*E*). At the end, we were able to model residues Val1-Val12 of XCL1 CC3 (residues in XCL1 CC3 and other chemokines are referred to by three-letter names, and residues in XCR1, G protein, and other GPCRs are referred to by one-letter names hereafter) in the structure based on the maps from overall and local refinements (Fig. 1 *D* and *E*). Most of the G_i protein heterotrimer is modeled except for the helical domain of $G_{\alpha i}$ due to the structural flexibility (42).

Binding of XCL1 CC3 to XCR1. One intriguing aspect of chemokine pharmacology is the "two-site" binding mechanism that chemokines employ to act on their specific receptors (34, 43–45). This involves an initial interaction of the core region of a chemokine with the extracellular N terminus of its receptor (Chemokine recognition site 1, CRS1), also referred to as the "docking" or "recognition" site. This first interaction facilitates the secondary binding of the N-terminal segment of the chemokine to the major orthosteric binding pocket in the 7-TM region (Chemokine recognition site 1, CRS2). The CRS2 binding allows the chemokine to make specific interactions with its receptor and cause conformational changes of the receptor, leading to receptor activation and downstream signaling through G_i or other signaling partners. For XCL1 CC3, since we could not model the core region, the molecular details of the CRS1 are still elusive.

The weak cryo-EM density of XCL1 CC3 core region implies a high flexibility of this region relative to the receptor (Fig. 1*E*). For other CC, CXC, and CX_3C chemokines, there are two cysteine residues at the N-terminal region mediating the formation of two disulfide bonds with the 30 s-loop and β3 regions, respectively (45), potentially stabilizing the core region relative to the N-terminal region in these chemokines (Fig. 1*A*). In XCL1, there is only one cysteine residue at the N terminus, Cys11, which forms a disulfide bond with Cys48 in the β3 strand (26, 35). The lack of the conserved disulfide bond with 30 s-loop in XCL1 (Fig. 1*A*) may result in increased flexibility of the core region relative to the N-terminal region, potentially accounting for the weak cryo-EM density of the core region of XCL1 CC3 in our structure. To further probe the conformational dynamics of XCL1 CC3 in the signaling complex, we modeled the structure of entire XCL1 CC3 bound to XCR1 using our structure as a template and performed molecular dynamics (MD) simulations on the complex (*SI Appendix*, Fig. S3). Indeed, the results indicate that the core region of XCL1 CC3 exhibits high flexibility relative to the receptor in the complex (*SI Appendix*, Fig. S3), consistent with the poor cryo-EM density of this region observed in our structure.

Among the N-terminal 12 residues from Val1 to Val12 of XCL1 CC3 modeled in the structure (Fig. 2*A*), the main chain of Arg9-Val12 engages in multiple hydrogen bonds with the main chain of XCR1 residues P21-N24, reminiscent of a β-strand motif (Fig. 2*B*). This site is similar to the chemokine recognition sites 1.5 (CRS1.5) identified in the structures of CXCR4 in complex with a viral chemokine, vMIP-II (46), and the viral chemokine receptor US28 in complex with CX_3CL1 (47). A turn of the XCL1 CC3 conformation at Lys8 allows its N-terminal segment to insert into the deep orthosteric CRS2 of XCR1 (Fig. 2*C* and *SI Appendix*, Fig. S4). Notably, within CRS2, there are sparse interactions between XCL1 CC3 and XCR1. Not all residues in the N-loop are involved in the direct interactions with the receptor. In the upper region of CRS2, the side chain of XCL1 CC3 Val5 forms hydrophobic interactions with XCR1 residues $W27^{1.28}$, $P90^{2.63}$, and $Y91^{2.64}$. In the lower region of CRS2, the amine group and the carbonyl group of Gly2 in XCL1 CC3 form hydrogen bonds with the side chains of XCR1 residues $Y241^{6.51}$ and $R273^{7.39}$ (Ballesteros-Weinstein numbering (48), respectively (Fig. 2*C*). In addition, the amine group of Val1 and the side chain of Glu4 in XCL1 CC3 form hydrogen bonds with the side chain and the main chain amine of XCR1 residue $Y177^{ECL2}$, respectively, and the side chain of XCL1 residue Ser3 forms a hydrogen bond with the side chain of XCR1 residue $N106^{3.29}$ (Fig. 2*C*). Besides those polar interactions, the side chain of XCL1 CC3 Val1 engages in hydrophobic interactions with XCR1 residues $V187^{5.40}$ and $L245^{6.55}$ at the bottom of the binding pocket (Fig. 2*C*). No other direct interactions are observed in this region.

Our structure largely agrees with previous studies on XCL1 variants (34). XCL1 Val1 and Ser3 form direct interactions with XCR1. Consequently, mutations of Val1 and Ser3 to Ala or the Val1 deletion could cause significantly decreased binding of XCL1 (34). In addition, Val1 and Gly2 are situated within a constricted space at the bottom of the binding pocket (*SI Appendix*, Fig. S4*A*). Introducing an additional N-terminal residue to Val1 or mutating Gly2 to Ala would lead to potential steric clash with nearby XCR1 residues, explaining the decreased potency of those XCL1 variants (34). XCL1 Glu4 has been suggested to be a critical residue in XCL binding (34). Indeed, we observe direct interactions between XCL1 CC3 Glu4 and XCR1 (Fig. 2*C*). On the other hand, mutating XCL1 Val5 to Ala did not substantially impact binding affinity of XCL1 (34). This implies that the hydrophobic interactions facilitated by XCL1 CC3 Val5 on the extracellular surface of the binding pocket (Fig. 2*C*) may not be important for the binding of XCL1.

We performed miniG_i and β-arrestin2 recruitment experiments to investigate the impact of mutations of XCR1 residues within the XCL1 CC3 binding pocket on the agonistic activity of XCL1 CC3 (Fig. 2*D* and *SI Appendix*, Fig. S5). Consistent with the insights derived from the cryo-EM structure, mutating key residues including $N106^{3.29}$, $V187^{5.40}$, $Y241^{6.51}$, and $L245^{6.55}$ in CRS2 that

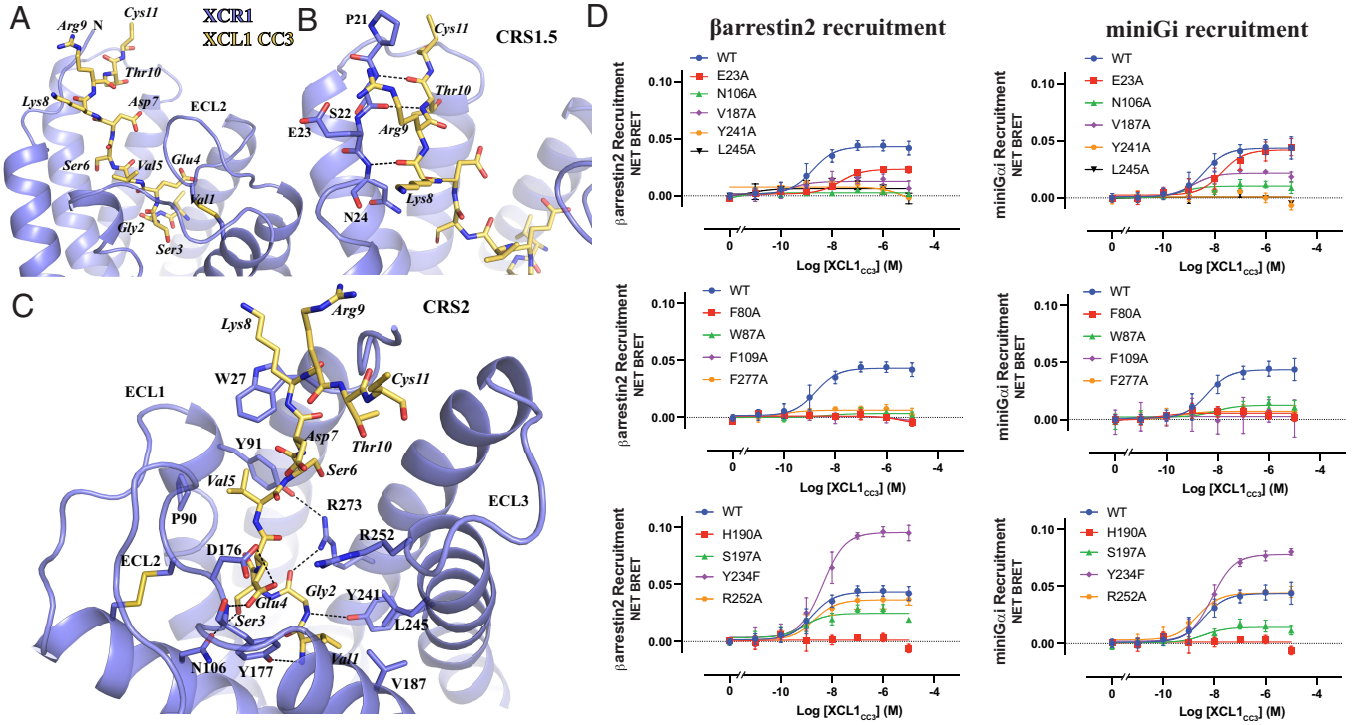

Fig. 2. XCL1 CC3 recognition. (*A*) Overall binding pose of Val1 to Cys11 of XCL1 CC3. XCL1 CC3 and XCR1 are colored in yellow and slate, respectively. (*B*) Interactions between XCL1 CC3 and XCR1 within CRS1.5. (*C*) Interactions between XCL1 CC3 and XCR1 within CRS2. In *A*–*C*, residues in XCL1 CC3 are labeled with three-letter names while residues in XCR1 are labeled with one-letter names. Hydrogen bonds are shown as black dash lines. (*D*) XCR1 mutations assessed for the agonistic activity of XCL1 CC3 in the recruitment of miniG$_i$ and β-arrestin2. The expression level of each mutant is shown in *SI Appendix*, Fig. S4. Data are means ± SEM. for n = 3 or more.

direct interact with XCL1 CC3 to Ala could either abolish the agonistic activity or significantly reduce the potency of XCL1 CC3 (Fig. 2*D* and *SI Appendix*, Fig. S5). Intriguingly, our mutagenesis studies also suggested that the alanine substitution of any of the four aromatic residues within the XCL1 CC3 binding pocket, F80$^{2.53}$, W87$^{2.60}$, F109$^{3.32}$, and F277$^{7.43}$, which do not directly interact with XCL1 CC3, had profound detrimental effects on the potency of XCL1 CC3 (Fig. 2*D* and *SI Appendix*, Fig. S4*B*). These four residues, together with W95^{ECL1}, are positioned along one side of the XCL1 CC3 binding pocket, forming an aromatic cluster (*SI Appendix*, Fig. S4*B*). It is plausible that this aromatic cluster contributes to shaping the overall structure of the XCL1 CC3 binding pocket. Introducing mutations in any of these residues is likely to disrupt the structural integrity of the binding pocket, subsequently impacting the binding of XCL1 CC3.

In previous computational docking study (34), we predicted that XCL1 Glu4 directly interacts with XCR1 residues Y177^{ECL2}, R252$^{6.62}$, and R273$^{7.39}$. However, contrary to the predicted XCL1 binding mode, the cryo-EM structure does not suggest direct polar interactions between XCL1 CC3 Glu4 and these polar residues of XCR1. Instead, in the cryo-EM structure, Y177^{ECL2} and R273$^{7.39}$ of XCR1 form hydrogen bonds with the main chain amine group of XCL1 CC3 Val1 and the carbonyl group of XCL1 CC3 Gly2, respectively. These findings align with our previous mutagenesis studies, where we showed that the Y177^{ECL2}A and R273$^{7.39}$A mutations resulted in significantly reduced XCL1 CC3 binding (34). On the other hand, in the cryo-EM structure, R252$^{6.62}$ is positioned distantly from XCL1 CC3 (Fig. 2*C*), with no direct interactions observed. Consistently, our mutagenesis studies showed that substituting R252$^{6.62}$ with Ala had only modest effects on the agonistic activity of XCL1 CC3 (Fig. 2*D*).

Structural Comparison of Chemokine Binding in XCR1 and Other Chemokine Receptors. The overall configuration and geometry of the chemokine binding pocket determines the specificity (43–45) or promiscuity (49) of chemokine binding. Structural comparison of XCR1 with the representative chemokine receptors CXCR2 (50), CX$_3$CR1 (37), and CCR5 (38, 51) from the CXCR, CX$_3$CR, and CCR classes, respectively, reveals largely similar extracellular regions with distinct conformations of TMs and ECLs. A noticeable difference is observed in the position of the extracellular region of TM6 in XCR1, which is more inwardly displaced compared to other chemokine receptors (*SI Appendix*, Fig. S6). Interestingly, the ECL2 in XCR1 is more similar to the ECL2 in CX$_3$CR, whereas the ECL2 in the other two receptors is significantly elongated (*SI Appendix*, Fig. S6). Moreover, while the conserved disulfide bond between TM3 and ECL2 is present in all four receptors, only CXCR2 and CCR5 but not CX$_3$CR or XCR1 possess an additional disulfide bond between the N terminus and the extracellular end of TM7 (*SI Appendix*, Fig. S5). These observations align with previous phylogenetic analyses of chemokine receptors, which indicate that CX$_3$CR is the closest phylogenetic neighbor to XCR1 (52).

In chemokines, the N-terminal amino acids occupy CRS2 to activate their receptors. Previous structural studies suggested a minor subpocket, primarily formed by TMs 1 to 2, and a major subpocket, primarily formed by TMs 4 to 6, within CRS2 (45). Various chemokines bind in CRS2 at different depths and form distinct interaction patterns within the major and minor subpockets, which are associated with different mechanisms of receptor activation (45). We compared the binding modes of the N-terminal regions up to the conserved N-terminal Cys residues of XCL1 CC3 (Cys11), CCL5 (Cys11), CXCL8 (Cys9), and

CX_3CL1 (Cys8) in their respective receptors XCR1, CCR5 (38), CXCR2 (50), and CX_3CR1 (37) (Fig. 3). The N-terminal regions of XCL1 CC3, CCL5, and CX_3CL1 penetrate CRS2 more deeply compared to that of CXCL8 (Fig. 3). In addition, while the N termini of XCL1 CC3, CCL5, and CX_3CL1 sample both major and minor subpockets, the CXCL8 N terminus predominantly occupies the major subpocket (Fig. 3). Upon closer examination, our structural comparison analysis suggested that the overall binding pose of the XCL1 N terminus exhibits a more pronounced resemblance to that of CX_3CL1 as opposed to the N termini in the other two chemokines. On the other hand, despite the similarity between XCL1 CC3 and CX_3CL1, the binding pocket of CX_3CL1 is significantly larger and more open than that of XCL1 CC3 (Fig. 3).

The distinct molecular features associated with XCL1 CC3 binding to XCR1, particularly the interactions of the XCL1 CC3 N-terminal region at the CRS2 of XCR1, appear to differ from those involved in other chemokine–receptor interactions. These unique features likely serve as molecular determinants for the specificity of the XCL1 CC3–XCR1 interaction. Both the length and amino acid composition of the XCL1 N terminus are crucial in determining its specificity as the XCR1 ligand. This is consistent with our previous studies on XCL1 variants, which demonstrated that alterations of the N-terminal residues Val1, Gly2, Ser3, and Glu4 of XCL1 could substantially affect receptor binding and/or receptor activation (34).

Activation of XCR1 Involving Distinctive Micromotifs. The active conformation of XCR1 highly resembles those of other G_i-coupled chemokine receptors such as CCR5(51) and CXCR2(50), especially within the cytoplasmic region, with the exception of CX_3CR1(37) (Fig. 4*A*). Structural alignment of active XCR1 and inactive CXCR4 bound to a chemokine antagonist, vMIP-II, showed inward rearrangements of TM5 and TM7 and an outward displacement of TM6 at the cytoplasmic region (Fig. 4*A*), which are characteristic of the active conformations of Class A GPCRs (53–56). In contrast, the conformation of G_i-coupled CX_3CR1 in the previously reported structure (37) mirrors that of inactive CXCR4 within the cytoplasmic region, especially for TM6 (Fig. 4*A*). The underlying mechanism for such a distinctive conformation of G_i-coupled CX_3CR1 may need further investigation.

To further investigate the activation mechanism of XCR1, we compared the structure of active XCR1 to the AlphaFold2-predicted inactive structure (AF structure) (57–60) of XCR1. Very subtle conformational differences are observed in the extracellular region (Fig. 4*B*). In the core region of 7-TM, an outward movement of TM6 at $L245^{6.55}$ and $Y241^{6.51}$ was observed, potentially due to steric effects with Val1 and Gly2 of XCL1 CC3 (Fig. 4*C*). Such a conformational change is associated with pronounced displacements of $W238^{6.48}$ and $Y234^{6.44}$ located at the core region of TM6 and even more significant displacements observed at the cytoplasmic end of TM6 (Fig. 4*B*). In addition to $L245^{6.55}$ and $Y241^{6.51}$, a large conformational change of $H190^{5.43}$ was also noted at the

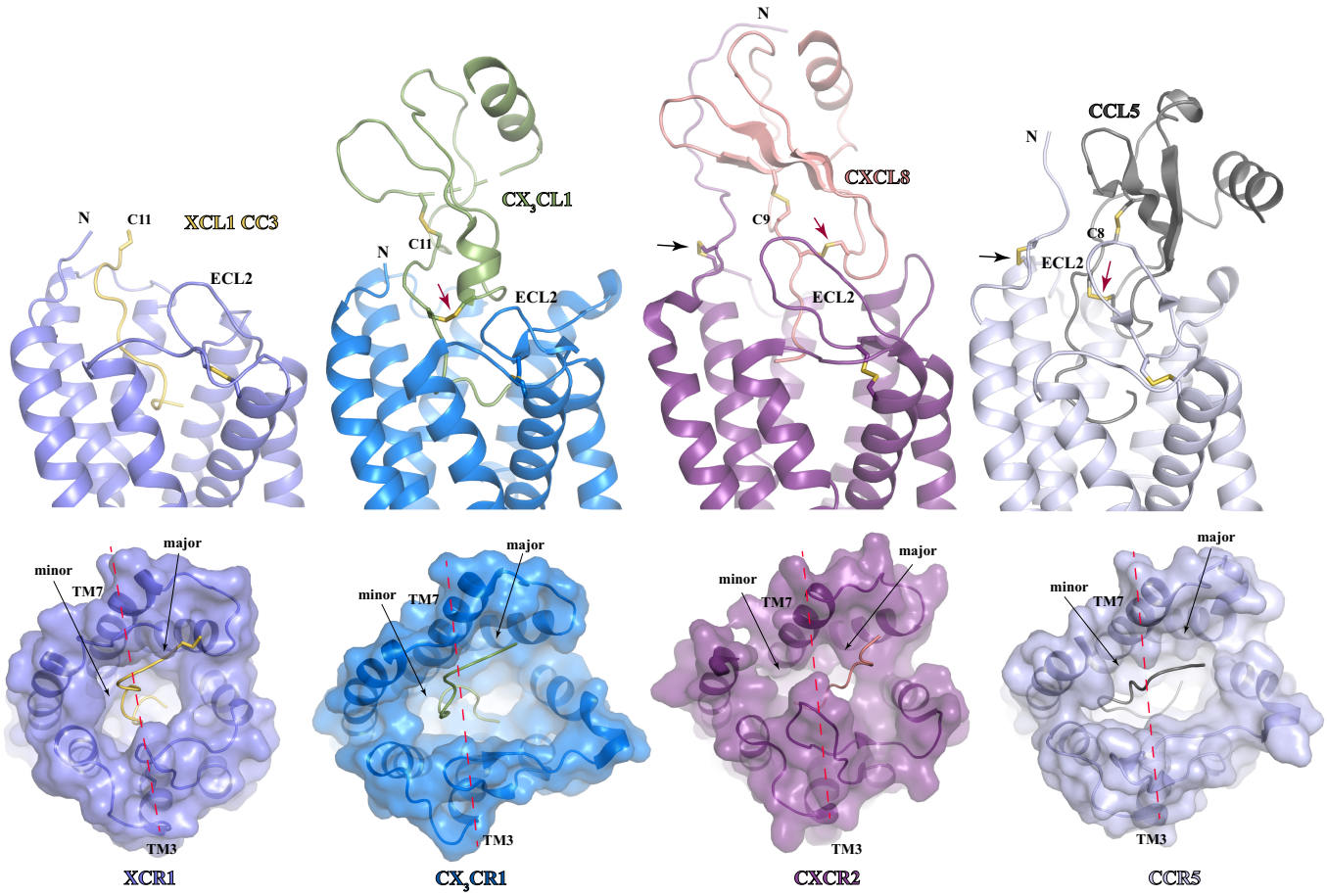

Fig. 3. Structural comparison of XCR1 with other chemokine receptors. The structures of four chemokine receptors, XCR1 (slate), CX_3CR1 (blue, PDB ID 7XBX), CXCR2 (purple, PDB ID 6LFO), and CCR5 (light blue, PDB ID 7O7F), in complexes with their respective chemokine ligands, XCL1 CC3 (yellow), CX_3CL1 (green), CXCL8 (salmon), and CCL5 (dark gray), are aligned. The chemokines belong to the C, CX_3C, CXC, and CC chemokine subfamilies, respectively, highlighting the specificity of receptor–chemokine interactions within these chemokine subfamilies. The red arrows point to the disulfide bonds linking the N-loop and the 30 s-loop within CX_3CL1, CXCL8, and CCL5, but not XCL1 CC3. The black arrows point to the disulfide bonds formed between the N-terminal region of the chemokine receptors and their ligands in CXCR2 and CCR5. In each receptor, the minor pocket and the major pocket are divided by the red dashed line.

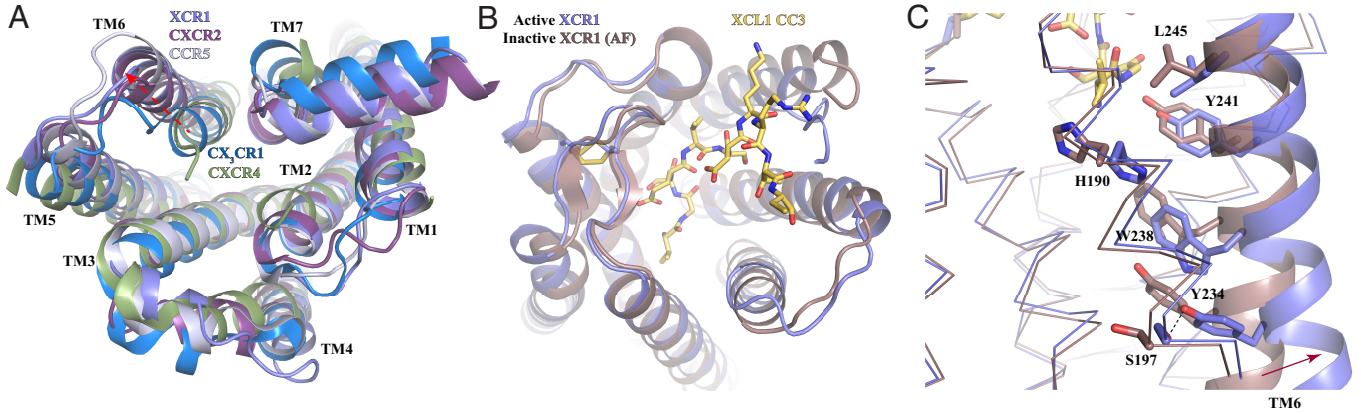

Fig. 4. XCR1 activation. (*A*) Structural comparison of the cytoplasmic regions in the G protein–coupled active XCR1 (slate), CXCR2 (purple), CCR5 (light blue), and CX_3CR1 (blue) and the inactive CXCR4 (green). The active conformation of CX_3CR1 resembles that of inactive CXCR4, especially for TM6. (*B*) and (*C*) Structural comparison of the extracellular region (*B*) and the core region (*C*) in the active G_i-coupled active XCR1 (slate) relative to them in the AlphaFold-predicted inactive XCR1 (brown). Different conformations of key residues in the core region of XCR1 that may be involved in receptor activation are shown in c. The red arrow indicates conformational changes of TM6. The black dashed line represents the hydrogen bond between $Y234^{6.44}$ and $S197^{5.50}$ in the active XCR1.

bottom of the ligand binding pocket, potentially due to steric effects with XCL1 CC3 (Fig. 4*C*). This shift may also be associated with the displacement of $W238^{6.48}$, which does not directly interact with XCL1 CC3. Therefore, we propose that Val1 and Gly2 of XCL1 CC3 at the bottom of the ligand binding pocket can induce an outward shift of TM6 due to steric effects with surrounding residues, thereby activating the receptor. Consistently, previous studies showed that mutations of Val1 and Gly2 of XCL1 CC3 to Ala or the deletion of Val1 could significantly compromise the agonistic action of XCL1 CC3 on XCR1 (34). Also, our mutagenesis data indicated that the H190A mutation nearly diminished the agonistic action of XCL1 CC3 in both miniG_i and β-arrestin2 recruitment assays without affecting the receptor expression level (Fig. 2*D* and *SI Appendix*, Fig. S5). It should be noted that the structures of inactive GPCRs predicted by AlphaFold might not be fully accurate. As such, our suggested activation mechanism for XCR1 remains a plausible hypothesis. Nevertheless, we simulated the AF structure of inactive XCR1 as well as the cryo-EM structure of the XCR1 signaling complex (*SI Appendix*, Fig. S7). Both structures remained stable throughout multiple MD simulations with critical residues in receptor activation including $L245^{6.55}$, $Y241^{6.51}$, and $H190^{5.43}$ showing minimal conformational dynamics (*SI Appendix*, Fig. S7), which may support the validity of using the AF structure of inactive XCR1 for our structural comparison analysis.

In most Class A GPCRs, TM6 features a highly conserved $F^{6.44}$xx$CW^{6.48}$xxP motif, which has been shown to play an important role in receptor activation (54). Specifically, $W^{6.48}$ and $F^{6.44}$ form a "transmission switch", linking receptor activation at the cytoplasmic region to the extracellular binding of agonists (54, 55, 61, 62). However, in XCR1, while $W^{6.48}$ is conserved, $F^{6.44}$ is substituted by $Y234^{6.44}$, and its side chain forms a hydrogen bond with $S197^{5.50}$ (Fig. 4*C*). Interestingly, the same $W^{6.48}/Y^{6.44}$ pair is also seen in the arginine vasopressin receptor V2R (63). Our mutagenesis studies showed that mutating $Y234^{6.44}$ to F, the more conserved residue at this position, increased the efficacy of XCL1 CC3 in both G_i and β-arrestin2 recruitment experiments assays (Fig. 2*D*). The underlying mechanism is not readily apparent. One possibility is that $Y234^{6.44}$ participates in some water-mediated polar interaction network in the inactive receptor, which helps to stabilize the inactive conformation (64). Mutating it to F could disrupt such network, potentially making the receptor easier to be activated.

Conserved G_i Binding Interface in XCR1. The overall XCR1 and G_i interface is similar to that observed in other G_i-coupled chemokine receptors such as CCR5 (51) and CXCR2 (50), with the exception of CX_3CR1 (37) (Fig. 5*A*). In the structure of G_i-coupled CX_3CR1, CX_3CR1 adopts an inactive-like conformation with potentially minor displacement of TM6 (Fig. 4*A*), resulting

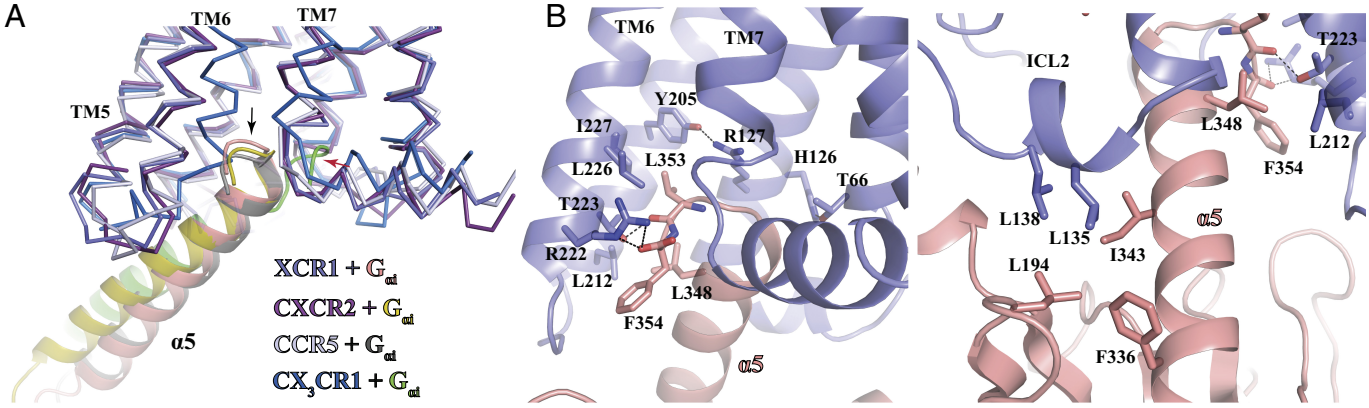

Fig. 5. G protein coupling. (*A*) Conserved and divergent features of G_i-coupling for XCR1 (slate), CX_3CR1 (blue, PDB ID 7XBX), CXCR2 (purple, PDB ID 6LF0), and CCR5 (light blue, PDB ID 7O7F). The $G_{\alpha i}$ subunit that is coupled to XCR1, CXCR2, CCR5, and CX_3CR1 is colored in salmon, yellow, dark gray, and green, respectively. The red arrow points to the wavy hook region at the end of the α5 helix of $G\alpha_i$ that is coupled to CX_3CR1. The black arrow points to the same region in $G\alpha_i$ that is coupled to other chemokine receptors. (*B*) Details of interactions between XCR1 and $G\alpha_i$. Hydrogen bonds are shown as black dashed lines.

in a cytoplasmic pocket with limited space for the coupling of $G\alpha_i$. Consequently, the wavy hook region at the end of the α5 helix of $G\alpha_i$ is too far away from TM5 and TM6 to form interactions with TMs 1, 2, and 7 (Fig. 5*A*), whereas in the structures of G_i-coupled XCR1 and other G_i-coupled chemokine receptors, the same region in $G\alpha_i$ is close to TM5 and TM6 of XCR1 and forms direct interactions with them (Fig. 5*A*).

In the structure of the XCR1–G_i complex, the C-terminal α5 of $G\alpha_i$ sticks into a pocket formed by the cytoplasmic ends of TMs 2, 3, 4, 5, and 7 of XCR1, forming the main interaction interface with the receptor (Fig. 5*B*). The conserved $DR^{3.50}Y$ motif at the cytoplasmic end of TM3 in most Class A GPCRs is replaced by an $HR^{3.50}Y$ motif in XCR1 (65). The same motif is also observed in the purinergic receptor $P2Y_1R$ (66). $H126^{3.49}$ and $R127^{3.50}$ in this motif form hydrogen bonds with the side chains of $T66^{2.39}$ and $Y205^{5.58}$, respectively, covering the pocket for the α5 of $G\alpha_i$ (Fig. 5*B*). The side chains of F354, L353, and L348 on one side of α5 of $G\alpha_i$ engage in hydrophobic interactions with XCR1 residues $L212^{5.65}$, $L226^{6.36}$, and $I227^{6.37}$, while the carboxylate group of F354 and the carbonyl group of L353 of $G\alpha_i$ form polar interactions with the side chains of XCR1 residues $R222^{6.32}$ and $T223^{6.33}$, respectively (Fig. 5*B*). In addition to the interactions in the α5 helix binding pocket, as for other G_i-coupled GPCRs, XCR1 also interacts with $G\alpha_i$ at ICL2. $L135^{ICL2}$ and $L138^{ICL2}$ of XCR1 form a hydrophobic cluster with L194 in the β2-β3 loop and F336 and I343 in the α5 helix of $G\alpha_i$ (Fig. 5*B*).

Discussion

As the only member of the C chemokine receptor family, XCR1 is a relatively understudied chemokine receptor. Nevertheless, the roles of XCL1–XCR1 signaling in regulating cDC1s and antigen presentation to different T cells have attracted much research interest in the past decade. We report a high-resolution structure of the XCR1-$G\alpha_i$ signaling complex with XCL1 CC3, which revealed the molecular details of the potential CRS1.5 and the orthosteric CRS2 in XCR1 for XCL1 CC3 and the interactions between XCL1 CC3 and XCR1 at these two sites. Structural comparison analysis indicates a distinctive binding pocket for XCL1 CC3, which differs from CRS2 in other chemokine receptors, elucidating the specificity of XCL1 recognition. The activation of XCR1 involves the conformational changes of residues $H190^{5.43}$, $L245^{6.55}$, and $Y241^{6.51}$ at the bottom of the XCL1 CC3 binding pocket, potentially due to steric effects with the N-terminal region of XCL1 CC3. The structural insights are validated by mutagenesis studies. It is worth noting that none of the mutations of XCR1 we have examined in both β-arrestin and mini$G_{\alpha i}$ recruitment assays exhibited significant signaling bias compared to the WT receptor when induced by XCL1 CC3 (*SI Appendix*, Fig. S8).

Given the central role of XCR1 in orchestrating immune responses, targeting this receptor may offer new opportunities in drug development aimed at modulating immune functions. For example, XCL1 has already demonstrated promising effects in enhancing immune responses to vaccines through the activation of XCR1 (67–69). In addition, activation of $XCR1^+$ DCs can promote the presentation of tumor antigens to CTLs, thereby potentially stimulating more robust anti-tumor immune responses. On the other hand, blocking XCR1 signaling may dampen overreactive immune responses in autoimmune diseases. Reducing the activity of $XCR1^+$ DCs may help induce tolerance to self-antigens and reduce the severity of autoimmune reactions. However, currently, no synthetic ligands functioning as either agonists or antagonists of XCR1 have been reported, which has greatly hindered the investigation of XCR1 pathophysiology. The minor and major subpockets of XCR1 revealed in our structure can be used to design synthetic ligands for XCR1. In addition, intracellular allosteric antagonists have also been identified for several CCRs including CCR2 (70) and CCR9 (71). In the cytoplasmic allosteric site of CCR2, residues $V^{6.36}$, $Y^{7.53}$, $K^{8.49}$, and $F^{8.50}$ are critical for the binding of the allosteric antagonist CCR2-RA-[*R*] and form hydrogen bonding or hydrophobic or π–π interactions with the ligand (70, 72). $Y^{7.53}$ is a part of the conserved $N/DP^{7.50}xxY^{7.53}$ motif in Class A GPCRs. Interestingly, all other three residues are conserved in XCR1, corresponding to XCR1 residues $L226^{6.36}$, $K293^{8.49}$, and $F294^{8.50}$. Therefore, it may be feasible to design intracellular antagonists for XCR1 as well. Targeting the chemokine receptor XCR1 holds significant therapeutic potential in a variety of diseases, from cancer to autoimmune diseases. While challenges exist, advancements in understanding the structure and pharmacology of this receptor are paving the way for innovative treatments that harness the power of the immune system. XCR1-targeted therapies may become an integral part of therapeutic methods against various diseases caused by a dysfunctional immune system.

Materials and Methods

Expression and Purification of XCL1 CC3 for BRET Assays. Recombinant XCL1 CC3 (V21C, V59C) used in the BRET experiments was expressed and purified similar to previously described methods (73). Briefly, XCL1 CC3 was expressed in BL21 (DE3) *Escherichia coli* cells transfected with a pET28a expression vector containing an N-terminal 6xHis-SUMO3 tag. Cells were grown at 37 °C in Luria-Bertani media containing 50 μg/mL kanamycin to an OD_{600} of 0.6 before induction with 1 mM isopropyl-β-D-thiogalactopyranoside (IPTG). The cultures were grown for an additional 5 h before the cells were pelleted by centrifugation at 5,000×*g* and stored at −20 °C.

Bacterial pellets were resuspended in lysis buffer (50 mM Na_2PO_4 (pH 8.0), 300 mM NaCl, 10 mM imidazole, 1 mM phenylmethylsulfonyl fluoride, and 0.1% (v/v) 2-mercaptoethanol (BME). Resuspended cells were lysed via sonication and clarified by centrifugation at 18,000×*g* for 20 min. The lysate supernatant was discarded, and the remaining insoluble pellet was dissolved in buffer AD (6 M guanidinium chloride, 50 mM Na_2PO_4 (pH 8.0), 300 mM NaCl, 10 mM imidazole) with 0.1% (v/v) 2-BME. The insoluble pellets were resuspended by sonication and again clarified by centrifugation at 18,000×*g* for 20 min. The resulting supernatant was loaded onto a 5 mL Ni-NTA column equilibrated in Buffer AD using an AKTA-Start system (GE Healthcare). The column was washed with Buffer AD, and terminal 6xHis-SUMO3-CC3 was eluted using Buffer BD (6 M guanidinium, 50 mM sodium acetate (pH 4.5), 300 mM NaCl, and 10 mM imidazole). CC3 was refolded overnight via drop-wise dilution into a sixfold greater volume of Refold Buffer (50 mM Na_2PO_4 (pH 7.4), 150 mM NaCl) with the addition of 10 mM cysteine, and 1 mM cystine. Refolded CC3 was concentrated in an Amicon Stirred Cell concentrator (Millipore Sigma) using a 10 kDa membrane. CC3 was added to 6 to 8 kDa dialysis tubing with the addition of ULP1 to cleave the N-terminal 6xHis-SUMO3-tag and dialyzed at 25 °C against Refold Buffer overnight. The AKTA-Start system was used to load the cleaved protein onto a 10 mL column of SP Sepharose Fast Flow resin (GE Healthcare) equilibrated in Refold Buffer. The column was washed with Cation Buffer A (50 mM Na_2PO_4 (pH 7.4), 150 mM NaCl), and CC3 was eluted using Cation Buffer B (50 mM Na_2PO_4 (pH 7.4), 2 M NaCl). XCL1 CC3 was purified to >99% homogeneity using reverse-phase high-performance liquid chromatography with a 60 min gradient from 30 to 60% acetonitrile with 0.1% TFA.

Expression and Purification of the XCL1 CC3–XCR1–Gi Complex. We designed a construct of WT human XCR1 fused with XCL1 CC3 and a 40-amino acid linker at its N-terminal end. We also added the signal peptide from bovine prolactin to the N-terminal end of XCL1 CC3, which is cleaved posttranslation, ensuring the exposure of the first N-terminal residue of XCL1 CC3. We also added the LargeBit protein along with an 8xHis tag and a FLAG tag to the C-terminal end of XCR1 to facilitate protein purification and complex formation (40). For the G_i protein, a dominant negative form of $G\alpha_{i1}$ ($DNG\alpha_{i1}$) with four mutations

(S47N, G203A, E245A, A326S) was used. Human $G_{\beta 1}$ was fused with an N-terminal 6xHis tag and a C-terminal HiBiT peptide (40) together a 15-amino acid linker. These proteins were cloned into the pFastBac vector for expression in insect cells using the baculovirus system (Fisher).

XCL1 CC3–XCR1, DNGα_{i1}, and G$\beta_1\gamma_2$ were coexpressed in Sf9 insect cells using the baculovirus method, as previously described in our earlier studies (74, 75). The three types of viruses were used to transfect Sf9 cells at the ratio of 1:1:1 for 48 h at 27 °C. After infection, cell pellets were collected by centrifugation and stored at −80 °C. Cell pellets were thawed in buffer containing 20 mM HEPES pH 7.5, 50 mM NaCl, 10 mM $MgCl_2$, 5 mM $CaCl_2$, 2.5 μg/mL leupeptin, and 300 μg/mL benzamidine. To facilitate complex formation, 25 mU/mL Apyrase (NEB) and 100 μM TCEP were added and incubated at room temperature for 2 h. The cell membranes were isolated by centrifugation at 25,000×*g* for 40 min and then resuspended in solubilization buffer containing 20 mM HEPES pH 7.5, 100 mM NaCl, 0.5% (w/v) lauryl maltose neopentylglycol (LMNG, Anatrace), 0.1% (w/v) cholesteryl hemisuccinate (CHS, Anatrace), 10% (v/v) glycerol, 10 mM $MgCl_2$, 5 mM $CaCl_2$, 12.5 mU/mL Apyrase, 2.5 μg/mL leupeptin, 300 μg/mL benzamidine, and 100 μM TECP for 2 h at 4 °C. After centrifugation at 25,000×*g* for 40 min, the supernatant was collected and then incubated with nickel resin at 4 °C overnight. The resin was washed with a buffer A containing 20 mM HEPES pH 7.5, 100 mM NaCl, 0.05% (w/v) LMNG, 0.01% (w/v) CHS, 20 mM imidazole, 2.5 μg/mL leupeptin, 300 μg/mL benzamidine, and 100 μM TECP. The complex was eluted with buffer A containing 400 mM imidazole. The eluate was loaded onto anti-Flag M2 antibody resin. After wash, the complex was eluted in buffer A containing 200 μg/mL FLAG peptide and concentrated using an Amicon Ultra Centrifugal Filter (MWCO, 100 kDa). Finally, a 1.3 molar excess of scFv16 was added to the elution. The sample was then loaded onto a Superdex 200 Increase 10/300 column (GE Healthcare) pre-equilibrated with buffer containing 20 mM HEPES pH 7.5, 100 mM NaCl, 0.00075% (w/v) LMNG, 0.00025% (w/v) GDN, 0.00015% (w/v) CHS and 100 μM TECP. Peak fractions of the complex were pooled and concentrated for cryo-EM experiments.

ScFv16 was expressed in Hi5 insect cells using Bac-to-Bac expression system. To purify the protein, the cell supernatant was collected and loaded onto Ni-NTA resins. Following nickel affinity chromatography, the protein was further subjected to size exclusion chromatography on a Superdex 200 Increase 100/300 GL column. The purified scFv16 was then collected and concentrated for complex assembly.

Cryo-EM Sample Preparation and Data Collection. The 3 μl protein sample was loaded to 1.2/1.3 UltrAufoil 300 mesh grids that had been plasma-cleaned and then plunged into liquid ethane using an FEI Vitrobot Mark IV (Thermo Fischer Scientific). 11,176 movies were collected using Titan Krios transmission electron microscope, equipped with a Falcon 4 Summit direct electron detector. Images were recorded with a nominal magnification of 96,000× using the EPU software with a calibrated pixel size of 0.82 Å and a defocus range of −1.0 to −2.0 μm. Each stack was dose-fractionated to 40 frames with a total dose of 55 $e^-/Å^2$.

Cryo-EM Data Processing. The cryo-EM data processing was done following a similar protocol outlined in our previous studies (74, 75). Movies were subjected to patch motion correction in cryoSPARC (76). Contrast transfer function (CTF) parameters were calculated using the patch CTF estimation tool. Total of 8,036,426 particles of XCL1 CC3–XCR1–G_i complex were autopicked and then subjected to 2D classification to discard bad particles. After ab initio reconstruction and heterogeneous refinement, 255,110 particles were subjected to nonuniform refinement, which generated a map with an indicated global resolution of 3.07 Å at a Fourier shell correlation of 0.143. The map was sharpened with deepEMhancer (77) and used for subsequent model building and analysis. To further improve quality of the XCR1 and XCL1 CC3, local refinement with a soft mask focusing on the receptor and peptide was performed in cryoSPARC. The focused refinement map for the XCR1 and XCL1 CC3 shows the indicated resolution of 3.99 Å, which was sharpened with deepEMhancer. Local resolution was estimated in cryoSPARC.

Model Building and Structure Refinement. The AlphaFold-predicted structure of XCR1 and structures of G_i and scFv16 obtained from the GPR84–G_i–scFv16 complex (PDB ID 8G05) were used as initial models for docking into the cryo-EM map using Chimera (78). The structure of XCL1 CC3–XCR1–G_i was subsequently generating using iterative manual building and adjustment in Coot (79), followed by real-space refinement in Phenix (80). The final model was validated by Molprobity. Detailed statistics for data collection, processing, and structure refinement statistics are provided in *SI Appendix*, Table S1.

Mutagenesis and BRET-Based Signaling Assays. BRET experiments were performed to provide a direct and high-throughput readout of receptor activity in response to functional mutants. We used methods similar to those used in our previous studies (81). The full-length sequence of XCR1 was cloned into a pcDNA3.1 vector to include an N-terminal HA-FLAG tag and a C-terminal IDTG linker proceeding the Rluc8 gene. Amino acid substitutions were made using Quikchange mutagenesis (Product Number: 200524 - Agilent). A pcDNA3.1 vector containing β-arrestin2 with an N-terminal Venus tag was used in this assay. The miniG_i construct was provided by the lab of Dr. Andy Chevigné and was cloned into the pcDNA3.1 Venus expression vector described above. HEK293T cells (ATCC) maintained in Dulbecco's modified Eagle's medium (DMEM) supplemented with 10% fetal bovine serum (FBS) were transiently transfected on 10 cm plates with 0.3 μg of XCR1-Rluc8 constructs and 5 μg of Venus-transducer at ~50% confluency using TransIT-293 (Mirus). At 24 h posttransfection, cells were resuspended in PBS supplemented with 0.1% glucose and plated in 96-well plates at a density of 100,000 cells/well in a total of 60 μL. After an additional 1 h at 37 °C, cells were stimulated with Coelenterazine-H to a final concentration of 5 μM and incubated for 5 min. XCL1 CC3 and vMIP-II were suspended in PBS supplemented with 0.1% glucose and were added at concentrations from 10 pM to 10 μM. WT-XCR1:CC3 was included in each plate as a positive control and BRET (540/480 nm) signals were measured upon CC3 addition on the Mithras LB940 (Berthold Technologies). Measurements on individual plates were performed in duplicate for each chemokine concentration. Data were analyzed with a nonlinear fit to create a dose–response curve in GraphPad Prism 10 (Graphpad Software Inc., San Diego, CA). Data from three independent plates were used in the analysis and calculation of SE. All data were baseline corrected to wells collected in the absence of chemokine. Mutant XCR1 expression levels were determined as the mean RLuc8 signal (480 nM) over three independent plates, normalized to WT XCR1.

Mutagenesis and BRET-Based Signaling Assays. BRET experiments were performed to provide a direct and high-throughput readout of receptor activity in response to functional mutants. We used methods similar to those used in our previous studies (81). The full-length sequence of XCR1 was cloned into a pcDNA3.1 vector to include an N-terminal HA-FLAG tag and a C-terminal IDTG linker proceeding the Rluc8 gene. Amino acid substitutions were made using Quikchange mutagenesis (Product Number: 200524 - Agilent). A pcDNA3.1 vector containing β-arrestin2 with an N-terminal Venus tag was used in this assay. The miniG_i construct was provided by the lab of Dr. Andy Chevigné and was cloned into the pcDNA3.1 Venus expression vector described above. HEK293T cells (ATCC) maintained in DMEM supplemented with 10% FBS were transiently transfected on 10 cm plates with 0.3 μg of XCR1-Rluc8 constructs and 5 μg of Venus-transducer at ~50% confluency using TransIT-293 (Mirus). At 24 h posttransfection, cells were resuspended in PBS supplemented with 0.1% glucose and plated in 96-well plates at a density of 100,000 cells/well in a total of 60 μL. After an additional 1 h at 37 °C, cells were stimulated with Coelenterazine-H to a final concentration of 5 μM and incubated for 5 min. XCL1 CC3 and vMIP-II were suspended in PBS supplemented with 0.1% glucose and were added at concentrations from 10 pM to 10 μM. WT-XCR1:CC3 was included in each plate as a positive control and BRET (540/480 nm) signals were measured upon CC3 addition on the Mithras LB940 (Berthold Technologies). Measurements on individual plates were performed in duplicate for each chemokine concentration. Data were analyzed with a nonlinear fit to create a dose–response curve in GraphPad Prism 10 (Graphpad Software Inc., San Diego, CA). Data from three independent plates were used in the analysis and calculation of SE. All data were baseline corrected to wells collected in the absence of chemokine. Mutant XCR1 expression levels were determined as the mean RLuc8 signal (480 nM) over three independent plates, normalized to WT XCR1.

Inactive XCR1 Modeling. A molecular model of the inactive XCR1 was generated with AlphaFold 2 using the ColabFold platform on Google Colaboratory. (57) The sequence of human XCR1 was obtained from UniProt (P46094)(82). The XCR1 sequence was submitted to ColabFold and the program was run without structural templates to enhance output heterogeneity. The sequence alignment

used MMseqs2 and UniRef90, and the value of pLDDT was used to rank the five resulting models. The top-ranked model was used as an input for MD simulations.

CC3–XCR1 Modeling. The full chemokine sequence of XCL1 V21C V59C (CC3) was modeled onto the cryoEM structure of CC3–XCR1–Galpha with AlphaFold 2 using the ColabFold platform on Google Colaboratory. The sequence of human XCL1 was obtained from UniProt and the V21C and V59C mutations were incorporated (P47992) (UniProt 2023). The sequences of CC3, XCR1, and GNAI were submitted to ColabFold in a hetero-oligomer format and the program was run using the XCR1 cryoEM structure as a structural template. The sequence alignment used MMseqs2 and UniRef90, and the value of ipTM was used to rank the five outputted models against one another.

After the conclusion of the modeling, the top-ranked AlphaFold complex was superimposed with the cryo-EM structure of XCR1 in PyMOL 3.0.3. The PDB files for the cryoEM structure and the AlphaFold complex were rewritten with the new superimposed coordinate system. Using these superimposed PDB files, the coordinates for residues 11–93 of CC3 were appended to the PDB file of the cryo-EM structure of XCR1, and the beta/gamma subunits were removed – providing a final input for MD simulations which included the full XCL1 CC3 structure.

MD Setup and Production. The MD inputs (described above) were uploaded to Charmm-GUI (charmm-gui.org) where the disulfides were reclassified, the membrane orientation was determined with PPM 2.0, and each model was placed into a synthetic biological membrane containing cholesterol, POPA, DDPC, DOPC, POPE, and POPS in a 6:2:2:8:6:1 ratio(83–88). Water, along with sodium and chloride ions at final concentrations of 150 mM, were then added to the system. After assembly, the system was downloaded in GROMACS format.

Each receptor underwent six rounds of equilibration at 310 K before triplicate 1 μs all-atom MD simulation using GROMACS 2021.2(89, 90) performed on the MCW Research Computing Center GPU server. All XCR1 models in this manuscript are snapshots of the MD simulation at 500 ns unless otherwise noted. All molecules were visualized with PyMOL 3.0.3.

MD Analysis. Principal Component Analysis (PCA) was used to reduce the MD data dimensionality and determine whether the active and inactive XCR1 were conformationally stable. This approach involves determining the eigenvalues of the mass-adjusted covariance matrix derived from the fluctuations in C-alpha x, y, and z positions. PCA was computed using SciKit-learn 1.5 and MDanalysis 2.0.0. Code available at https://www.mdanalysis.org (91). A concatenated trajectory was used as an input. This trajectory contained only XCR1 coordinates from each inactive and active MD run. The results of this analysis are shown in *SI Appendix*, Fig. S7*A* for PC1 and PC2.

RMSD of the triplicate CC3–XCR1-GNAI trajectories was calculated for XCR1 alone and for the CC3–XCR1 complex using GROMACS 2021.2. Each simulation was aligned to the input structure, and the backbone RMSD was calculated for each frame (2,501 frames in total) of the 1 μsecond simulation. The results are shown in *SI Appendix*, Fig. S3*B*.

Data, Materials, and Software Availability. The 3D cryo-EM density map of the XCL1 CC3–XCR1–Gi complex has been deposited in the Electron Microscopy Data Bank under the accession code: EMD-43825 (92). Atomic coordinates for the atomic model have been deposited in the Protein Data Bank (PDB) under the accession code: 9AST (93).

ACKNOWLEDGMENTS. We thank the cryo-EM facility at the University of Pittsburgh partly supported by the grants S10 OD025009 (Krios) and S10 OD019995 (Falcon 2/3 camera) from the NIH in the USA. We thank Dr. James Conway at the University of Pittsburgh for oversight of the cryo-EM core facility and help with cryo-EM data collection. We thank Dr. J. Silvio Gutkind from the University of California San Diego, School of Medicine for valuable discussions on the project. This work was supported by the NIH grant R35GM128641 to C.Z. and by NIH grants R01 AI168423 and R37 AI058072 to B.F.V. This research was completed in part with computational resources and technical support provided by the Research Computing Center at the Medical College of Wisconsin.

Author affiliations: [a]Department of Pharmacology and Chemical Biology, School of Medicine, University of Pittsburgh, Pittsburgh, PA 15261; [b]Department of Biochemistry, Medical College of Wisconsin, Milwaukee, WI 53226; and [c]Program in Chemical Biology, Medical College of Wisconsin, Milwaukee, WI 53226

1. A. Gardner, A. de Mingo Pulido, B. Ruffell, Dendritic cells and their role in immunotherapy. *Front. Immunol.* **11**, 924 (2020).
2. S. K. Wculek *et al.*, Dendritic cells in cancer immunology and immunotherapy. *Nat. Rev. Immunol.* **20**, 7–24 (2020).
3. B. G. Dorner *et al.*, Selective expression of the chemokine receptor XCR1 on cross-presenting dendritic cells determines cooperation with CD8+ T cells. *Immunity* **31**, 823–833 (2009).
4. A. Bachem *et al.*, Superior antigen cross-presentation and XCR1 expression define human CD11c+CD141+ cells as homologues of mouse CD8+ dendritic cells. *J. Exp. Med.* **207**, 1273–1281 (2010).
5. A. Bachem *et al.*, Expression of XCR1 characterizes the Batf3-dependent lineage of dendritic cells capable of antigen cross-presentation. *Front. Immunol.* **3**, 214 (2012).
6. C. Yamazaki *et al.*, Critical roles of a dendritic cell subset expressing a chemokine receptor, XCR1. *J. Immunol.* **190**, 6071–6082 (2013).
7. E. Hartung *et al.*, Induction of potent CD8 T cell cytotoxicity by specific targeting of antigen to cross-presenting dendritic cells in vivo via murine or human XCR1. *J. Immunol.* **194**, 1069–1079 (2015).
8. A. R. Sanchez-Paulete *et al.*, Intratumoral Immunotherapy with XCL1 and sFlt3L encoded in recombinant semliki forest virus-derived vectors fosters dendritic cell–mediated T-cell cross-priming. *Cancer Res.* **78**, 6643–6654 (2018).
9. H. Salmon *et al.*, Expansion and activation of CD103(+) dendritic cell progenitors at the tumor site enhances tumor responses to therapeutic PD-L1 and BRAF inhibition. *Immunity* **44**, 924–938 (2016).
10. M. L. Broz *et al.*, Dissecting the tumor myeloid compartment reveals rare activating antigen-presenting cells critical for T cell immunity. *Cancer Cell* **26**, 938 (2014).
11. X. Yin, S. Chen, S. C. Eisenbarth, Dendritic cell regulation of T helper cells. *Annu. Rev. Immunol.* **39**, 759–790 (2021).
12. S. T. Ferris *et al.*, cDC1 prime and are licensed by CD4(+) T cells to induce anti-tumour immunity. *Nature* **584**, 624–629 (2020).
13. K. Crozat *et al.*, The XC chemokine receptor 1 is a conserved selective marker of mammalian cells homologous to mouse CD8alpha+ dendritic cells. *J. Exp. Med.* **207**, 1283–1292 (2010).
14. T. Yoshida *et al.*, Identification of single C motif-1/lymphotactin receptor XCR1. *J. Biol. Chem.* **273**, 16551–16554 (1998).
15. J. P. Bottcher *et al.*, NK cells stimulate recruitment of cDC1 into the tumor microenvironment promoting cancer immune control. *Cell* **172**, 1022–1037.e1014 (2018).
16. R. A. Kroczek, V. Henn, The role of XCR1 and its ligand XCL1 in antigen cross-presentation by murine and human dendritic cells. *Front. Immunol.* **3**, 14 (2012).
17. L. Heger *et al.*, XCR1 expression distinguishes human conventional dendritic cell type 1 with full effector functions from their immediate precursors. *Proc. Natl. Acad. Sci. U.S.A.* **120**, e2300343120 (2023).
18. R. F. Rousseau *et al.*, Local and systemic effects of an allogeneic tumor cell vaccine combining transgenic human lymphotactin with interleukin-2 in patients with advanced or refractory neuroblastoma. *Blood* **101**, 1718–1726 (2003).
19. X. L. Sheng, H. Zhang, In-vitro activation of cytotoxic T lymphocytes by fusion of mouse hepatocellular carcinoma cells and lymphotactin gene-modified dendritic cells. *World J. Gastroenterol.* **13**, 5944–5950 (2007).
20. D. Terhorst *et al.*, Laser-assisted intradermal delivery of adjuvant-free vaccines targeting XCR1+ dendritic cells induces potent antitumoral responses. *J. Immunol.* **194**, 5895–5902 (2015).
21. H. V. Russell *et al.*, Phase I trial of vaccination with autologous neuroblastoma tumor cells genetically modified to secrete IL-2 and lymphotactin. *J. Immunother.* **30**, 227–233 (2007).
22. F. Markl, D. Huynh, S. Endres, S. Kobold, Utilizing chemokines in cancer immunotherapy. *Trends Cancer* **8**, 670–682 (2022).
23. A. J. Stephens, N. A. Burgess-Brown, S. Jiang, Beyond just peptide antigens: The complex world of peptide-based cancer vaccines. *Front. Immunol.* **12**, 696791 (2021).
24. B. Dorner *et al.*, Purification, structural analysis, and function of natural ATAC, a cytokine secreted by CD8(+) T cells. *J. Biol. Chem.* **272**, 8817–8823 (1997).
25. C. E. Hughes, R. J. B. Nibbs, A guide to chemokines and their receptors. *FEBS J.* **285**, 2944–2971 (2018).
26. E. S. Kuloglu *et al.*, Monomeric solution structure of the prototypical "C" chemokine lymphotactin. *Biochemistry* **40**, 12486–12496 (2001).
27. E. S. Kuloglu, D. R. McCaslin, J. L. Markley, B. F. Volkman, Structural rearrangement of human lymphotactin, a C chemokine, under physiological solution conditions. *J. Biol. Chem.* **277**, 17863–17870 (2002).
28. R. L. Tuinstra *et al.*, Interconversion between two unrelated protein folds in the lymphotactin native state. *Proc. Natl. Acad. Sci. U.S.A.* **105**, 5057–5062 (2008).
29. A. F. Dishman *et al.*, Evolution of fold switching in a metamorphic protein. *Science* **371**, 86–90 (2021).
30. N. F. Neel, E. Schutyser, J. Sai, G. H. Fan, A. Richmond, Chemokine receptor internalization and intracellular trafficking. *Cytokine Growth Factor Rev.* **16**, 637–658 (2005).
31. K. A. DeFea, Stop that cell! Beta-arrestin-dependent chemotaxis: a tale of localized actin assembly and receptor desensitization *Annu. Rev. Physiol.* **69**, 535–560 (2007).
32. A. Bauer *et al.*, Rat cytomegalovirus-encoded gamma-chemokine vXCL1 is a highly adapted, species-specific agonist for rat XCR1-positive dendritic cells. *J. Cell Sci.* **133**, jcs236190
33. A. L. Kroczek *et al.*, Structure-function relationship of XCL1 used for in vivo targeting of antigen Into XCR1(+) dendritic cells. *Front. Immunol.* **9**, 2806 (2018).
34. J. C. Fox *et al.*, Structure-function guided modeling of chemokine-GPCR specificity for the chemokine XCL1 and its receptor XCR1. *Sci. Signal* **12**, eaat4128 (2019).
35. R. L. Tuinstra, F. C. Peterson, E. S. Elgin, A. J. Pelzek, B. F. Volkman, An engineered second disulfide bond restricts lymphotactin/XCL1 to a chemokine-like conformation with XCR1 agonist activity. *Biochemistry* **46**, 2564–2573 (2007).
36. R. Nehme *et al.*, Mini-G proteins: Novel tools for studying GPCRs in their active conformation. *PLoS One* **12**, e0175642 (2017).

37. M. Lu *et al.*, Activation of the human chemokine receptor CX3CR1 regulated by cholesterol. *Sci. Adv.* **8**, eabn8048 (2022).
38. H. Zhang *et al.*, Structural basis for chemokine recognition and receptor activation of chemokine receptor CCR5. *Nat. Commun.* **12**, 4151 (2021).
39. Y. L. Liang *et al.*, Dominant negative G proteins enhance formation and purification of agonist-GPCR-G Protein complexes for structure determination. *ACS Pharmacol. Transl. Sci.* **1**, 12–20 (2018).
40. J. Duan *et al.*, Cryo-EM structure of an activated VIP1 receptor-G protein complex revealed by a NanoBiT tethering strategy. *Nat. Commun.* **11**, 4121 (2020).
41. A. Koehl *et al.*, Structure of the micro-opioid receptor-Gi protein complex. *Nature* **558**, 547–552 (2018).
42. A. M. Preininger, J. Meiler, H. E. Hamm, Conformational flexibility and structural dynamics in GPCR-mediated G protein activation: A perspective. *J. Mol. Biol.* **425**, 2288–2298 (2013).
43. L. Rajagopalan, K. Rajarathnam, Structural basis of chemokine receptor function–a model for binding affinity and ligand selectivity. *Biosci. Rep.* **26**, 325–339 (2006).
44. M. Arimont *et al.*, Structural analysis of chemokine receptor-ligand interactions. *J. Med. Chem.* **60**, 4735–4779 (2017).
45. A. B. Kleist *et al.*, New paradigms in chemokine receptor signal transduction: Moving beyond the two-site model. *Biochem. Pharmacol.* **114**, 53–68 (2016).
46. L. Qin *et al.*, Structural biology crystal structure of the chemokine receptor CXCR4 in complex with a viral chemokine. *Science* **347**, 1117–1122 (2015).
47. J. S. Burg *et al.*, Structural biology structural basis for chemokine recognition and activation of a viral G protein-coupled receptor. *Science* **347**, 1113–1117 (2015).
48. J. A. Ballesteros, H. Weinstein, Integrated methods for the construction of three-dimensional models and computational probing of structure-function relations in G protein-coupled receptors. *Methods Neurosci.* **25**, 366–428 (1995).
49. T. F. Miles *et al.*, Viral GPCR US28 can signal in response to chemokine agonists of nearly unlimited structural degeneracy. *Elife* **7**, e35850 (2018).
50. K. Liu *et al.*, Structural basis of CXC chemokine receptor 2 activation and signalling. *Nature* **585**, 135–140 (2020).
51. P. Isaikina *et al.*, Structural basis of the activation of the CC chemokine receptor 5 by a chemokine agonist. *Sci. Adv.* **7**, eabg8685 (2021).
52. A. Zlotnik, O. Yoshie, H. Nomiyama, The chemokine and chemokine receptor superfamilies and their molecular evolution. *Genome Biol.* **7**, 243 (2006).
53. Q. Zhou *et al.*, Common activation mechanism of class A GPCRs. *eLife* **8**, e50279 (2019).
54. W. I. Weis, B. K. Kobilka, The molecular basis of G protein-coupled receptor activation. *Annu. Rev. Biochem.* **87**, 897–919 (2018).
55. A. Manglik, A. C. Kruse, Structural basis for G protein-coupled receptor activation. *Biochemistry* **56**, 5628–5634 (2017).
56. A. Glukhova *et al.*, Rules of engagement: GPCRs and G proteins. *ACS Pharmacol. Transl. Sci.* **1**, 73–83 (2018).
57. J. Jumper *et al.*, Highly accurate protein structure prediction with AlphaFold. *Nature* **596**, 583–589 (2021).
58. K. Tunyasuvunakool *et al.*, Highly accurate protein structure prediction for the human proteome. *Nature* **596**, 590–596 (2021).
59. L. Heo, M. Feig, Multi-state modeling of G-protein coupled receptors at experimental accuracy. *Proteins* **90**, 1873–1885 (2022).
60. G. Pandy-Szekeres *et al.*, GPCRdb in 2023: State-specific structure models using AlphaFold2 and new ligand resources. *Nucleic Acids Res.* **51**, D395–D402 (2023).
61. X. Deupi, J. Standfuss, Structural insights into agonist-induced activation of G-protein-coupled receptors. *Curr. Opin. Struct. Biol.* **21**, 541–551 (2011).
62. B. Trzaskowski *et al.*, Action of molecular switches in GPCRs–theoretical and experimental studies. *Curr. Med. Chem.* **19**, 1090–1109 (2012).
63. L. Wang *et al.*, Cryo-EM structure of the AVP-vasopressin receptor 2-G(s) signaling complex. *Cell Res.* **31**, 932–934 (2021).
64. A. J. Venkatakrishnan *et al.*, Diverse GPCRs exhibit conserved water networks for stabilization and activation. *Proc. Natl. Acad. Sci. U.S.A.* **116**, 3288–3293 (2019).
65. L. Y. Ni *et al.*, Identification and expression analysis of three XCR1-like receptors from Epinephelus coioides after Cryptocaryon irritans infection. *Fish Shellfish Immunol.* **67**, 95–102 (2017).
66. A. Neumann, C. E. Muller, V. Namasivayam, P2Y(1)-like nucleotide receptors-Structures, molecular modeling, mutagenesis, and oligomerization. *Wires Comput. Mol. Sci.* **10**, 1464 (2020).
67. E. Fossum *et al.*, Vaccine molecules targeting Xcr1 on cross-presenting DCs induce protective CD8+ T-cell responses against influenza virus. *Eur. J. Immunol.* **45**, 624–635 (2015).
68. H. Qi, Z. Sun, Y. Yao, L. Chen, X. Su, Immunogenicity of the Xcl1-SARS-CoV-2 spike fusion DNA vaccine for COVID-19. *Vaccines (Basel)* **10**, 407 (2022).
69. A. Gudjonsson, T. K. Andersen, V. Sundvold-Gjerstad, B. Bogen, E. Fossum, Endocytosis deficient murine Xcl1-fusion vaccine enhances protective antibody responses in mice. *Front. Immunol.* **10**, 1086 (2019).
70. Y. Zheng *et al.*, Structure of CC chemokine receptor 2 with orthosteric and allosteric antagonists. *Nature* **540**, 458–461 (2016).
71. C. Oswald *et al.*, Intracellular allosteric antagonism of the CCR9 receptor. *Nature* **540**, 462–465 (2016).
72. A. J. Zweemer *et al.*, Discovery and mapping of an intracellular antagonist binding site at the chemokine receptor CCR2. *Mol. Pharmacol.* **86**, 358–368 (2014).
73. J. C. Fox *et al.*, Structural and agonist properties of XCL2, the other member of the C-chemokine subfamily. *Cytokine* **71**, 302–311 (2015).
74. X. Zhang *et al.*, Structural basis of G protein-coupled receptor CMKLR1 activation and signaling induced by a chemerin-derived agonist. *PLoS Biol.* **21**, e3002188 (2023).
75. X. Zhang *et al.*, Structural basis for the ligand recognition and signaling of free fatty acid receptors. *Sci. Adv.* **10**, eadj2384 (2024).
76. A. Punjani, J. L. Rubinstein, D. J. Fleet, M. A. Brubaker, cryoSPARC: Algorithms for rapid unsupervised cryo-EM structure determination. *Nat. Methods* **14**, 290–296 (2017).
77. R. Sanchez-Garcia *et al.*, DeepEMhancer: A deep learning solution for cryo-EM volume post-processing. *Commun. Biol.* **4**, 874 (2021).
78. E. F. Pettersen *et al.*, UCSF ChimeraX: Structure visualization for researchers, educators, and developers. *Protein Sci.* **30**, 70–82 (2021).
79. P. Emsley, K. Cowtan, Coot: model-building tools for molecular graphics. *Acta Crystallogr. D Biol. Crystallogr.* **60**, 2126–2132 (2004).
80. P. D. Adams *et al.*, PHENIX: A comprehensive Python-based system for macromolecular structure solution. *Acta Crystallogr. D Biol. Crystallogr.* **66**, 213–221 (2010).
81. R. R. Schlimgen *et al.*, Structural basis for selectivity and antagonism in extracellular GPCR-nanobodies. *Nat. Commun.* **15**, 4611 (2024).
82. C. UniProt, UniProt: The universal protein knowledgebase in 2023. *Nucleic Acids Res.* **51**, D523–D531 (2023).
83. S. Jo, T. Kim, W. Im, Automated builder and database of protein/membrane complexes for molecular dynamics simulations. *PLoS One* **2**, e880 (2007).
84. S. Jo, T. Kim, V. G. Iyer, W. Im, CHARMM-GUI: A web-based graphical user interface for CHARMM. *J. Comput. Chem.* **29**, 1859–1865 (2008).
85. S. Jo, J. B. Lim, J. B. Klauda, W. Im, CHARMM-GUI membrane builder for mixed bilayers and its application to yeast membranes. *Biophys. J.* **97**, 50–58 (2009).
86. J. Lee *et al.*, CHARMM-GUI Input Generator for NAMD, GROMACS, AMBER, OpenMM, and CHARMM/OpenMM simulations using the CHARMM36 additive force field. *J. Chem. Theory Comput.* **12**, 405–413 (2016).
87. J. Lee *et al.*, CHARMM-GUI membrane builder for complex biological membrane simulations with glycolipids and lipoglycans. *J. Chem. Theory Comput.* **15**, 775–786 (2019).
88. E. L. Wu *et al.*, CHARMM-GUI membrane builder toward realistic biological membrane simulations. *J. Comput. Chem.* **35**, 1997–2004 (2014).
89. S. Pall *et al.*, Heterogeneous parallelization and acceleration of molecular dynamics simulations in GROMACS. *J. Chem. Phys.* **153**, 134110 (2020).
90. D. Van Der Spoel *et al.*, GROMACS: Fast, flexible, and free. *J. Comput. Chem.* **26**, 1701–1718 (2005).
91. N. Michaud-Agrawal, E. J. Denning, T. B. Woolf, O. Beckstein, MDAnalysis: A toolkit for the analysis of molecular dynamics simulations. *J. Comput. Chem.* **32**, 2319–2327 (2011).
92. X. Zhang *et al.*, Cryo-EM structure of XCR1 signaling complex. EMDB database. https://www.ebi.ac.uk/emdb/EMD-43825. Deposited 26 February 2024.
93. X. Zhang *et al.*, Cryo-EM structure of XCR1 signaling complex. PDB database. http://doi.org/10.2210/pdb9AST/pdb. Deposited 26 February 2024.